Supplementary Information

Design of Multi-Single-Atom Alloys for Tandem CH_4 Conversion

Rui Qi,[a,b] Beien Zhu[a,b*] and Yi Gao[a,b*]

a Photon Science Research Center for Carbon Dioxide, Shanghai Advanced Research Institute, Chinese Academy of Sciences, Shanghai 201210, China

b Key Laboratory of Low-Carbon Catalysis and Carbon Dioxide Utilization, Shanghai Advanced Research Institute, Chinese Academy of Sciences, Shanghai 201210, China

Computational details

DFT methods

All spin-polarized DFT calculations were performed using the Vienna ab initio Simulation Package (VASP) version 5.4.4.[1,2] The Perdew-Burke-Ernzerhof (PBE) exchange-correlation functional together with Grimme's D3 dispersion correction was employed.[3,4] The core-valence interactions were modeled using the projector-augmented wave (PAW) method with a kinetic energy cutoff of 520 eV.[5,6] We used a 3 × 3 supercell with nine atomic layers (96 atoms) to model surfaces for assessing the stability of SAAs, and a 4 × 4 supercell with six atomic layers to analyze the tandem reaction pathways of methane conversion. To eliminate interactions between periodic images, a vacuum region of 15 Å was introduced. The atoms in the two bottommost layers of the 3 × 3 nine-layer and 4 × 4 four-layer slabs were fixed. And other atom layers, as well as all adsorbed species, were relaxed. A Monkhorst-Pack grid of 2 × 2 × 1 was used to sample the Brillouin zone for the periodic slabs.[7] Geometry optimizations were carried out with convergence criteria of 0.02 eV/Å for atomic forces and 10^{-5} eV for total energy changes.

Aggregation energy and segregation energy were evaluated as key metrics for predicting the stability of MSAAs. Aggregation energy quantifies the tendency of an isolated dopant atom to form clusters on the host metal surface to access the relative stability against aggregation and was computed using: [8-10]

$$\Delta E_{agg} = E_{2SA\_Surface} + E_{Surface} - 2 \times E_{SAA\_Surface}$$

where $E_{2SA\_Surface}$ is the total energies of dopant dimer embedded on the alloy surface, $E_{Surface}$ represents the host surface, and $E_{SAA\_Surface}$ is the surface with doped single-atom, respectively. For the heteronuclear Pd–Rh pair, the aggregation energy was defined as：

$$\Delta E_{agg} = E_{PdRh\_Au111} + E_{Au111} - E_{Pd\_Au111} - E_{Rh\_Au111}$$

where E_{PdRh_Au111} is the total energy of the co-doped surface with adjacent Pd and Rh atoms, E_{Pd_Au111} and E_{Rh_Au111} are the total energies of the isolated single-atom alloy surfaces, respectively, and E_{Au111} is the total energy of the pristine Au (111) slab. A positive value indicates that the dispersed configuration is thermodynamically favored over aggregation. Segregation energy measures the stability of a dopant atom at the surface versus in the bulk and was calculated by: [8-10]

$$\Delta E_{seg} = E_{SA\_Bulk} - E_{SA\_Surface}$$

in which E_{SA_Bulk} and $E_{SA\_Surface}$ are the total energies of the systems with the dopant immersed in the 5th layer of the host material slab and the single dopant atom in the surface, respectively. A positive segregation energy and a positive aggregation energy

together provide a thermodynamic criterion for the formation of a single-atom alloy. Considering that the catalyst must remain stable under the reaction, the gas-induced segregation should also be considered and is therefore given as:[9]

$$\Delta E_{seg}^{gas} = \Delta E_{seg} + (E_{ads}^{host}(gas) - E_{ads}^{SAA}(gas))$$

where $E_{ads}^{host}(gas)$ and $E_{ads}^{SAA}(gas)$ represents the adsorption energy of gas on the host slab and SAA surface, respectively. Given the high activity of single-atom alloys (SAAs) in the hydrogen evolution reaction,[11] the gas is only O_2 and CH_4. A positive ΔE_{seg}^{gas} means the stable MSAA under tandem reaction. We optimized the minimum energy paths (MEPs) for tandem reaction-the first step is the generation of in-situ H_2O_2 with O_2 and the following is the conversion of CH_4 to CH_3OH-using the climbing image nudged elastic band (CI-NEB) method with the quasi-Newton algorithm.[12] Vibrational frequencies of the optimized structures were computed using the finite difference method with a step size of 0.02 Å.

The ab initio molecular dynamics (AIMD) simulations were conducted in the canonical (NVT) ensemble using a Nosé-Hoover thermostat to maintain the system temperature at 500 K. A plane-wave cutoff energy of 520 eV and a single gamma point were employed for Brillouin zone integration to balance computational efficiency and accuracy. The convergence criterion for the electronic self-consistent loop was set to 10^{-5} eV. Real-space projection operators were used to accelerate the evaluation of non-local pseudopotential contributions. The equations of motion were integrated using a time step of 1.0 fs, and each system was simulated for a total of 10,000 steps, yielding a 10 ps trajectory for subsequent structural and dynamic analyses.

Subgroup discovery

The SGD was performed with the RealKD code (https://bitbucket.org/realKD/realkd/). We applied the 15-means algorithm to cluster each feature into 15 groups. The resulting inter-cluster boundaries (a1, a2, ...) formed the basis for constructing inequalities (feature1 < a1), (feature2 $\geqslant$ a2), and so forth. While the final results can vary with the number of clusters, prior research indicates that employing a relatively high number yields broadly consistent findings.[13] Candidate subgroups are constructed as combinations of simple inequalities. The kernel of SGD is that subgroups are distinctive when the data distribution within them significantly deviates from the whole sampling. In this work, the data distribution refers to the distribution of a target property (E_{Stable} and E_{ads}). The uniqueness is assessed using a quality function for maximizing E_{Stable} or minimizing E_{ads}:

$$Q_{max}(S) = \frac{s(S)}{s(P)}\left(\frac{\min(S) - \min(P)}{\max(P) - \min(P)}\right)\theta(\min(S) - c)$$

$$Q_{min}(S) = \frac{s(S)}{s(P)}\left(\frac{\max(S) - \max(P)}{\max(P) - \min(P)}\right)(c - \max(S))$$

The variables used in the function include S for subgroup, P for the entire sample, s

for size, max and min denote the maximum and minimum values of target property, c is the cutoff of the target property, and θ is the Heaviside function. A Monte Carlo scheme, customized for this task, was utilized to identify subgroups. The procedure initiated with the generation of a specific quantity of trial conjunctions (seeds). Subsequently, the quality function was evaluated for each seed, incorporating the pruning of inequalities. Based on this evaluation, subgroups arising from 200,000 seeds that showed high convergence precision were chosen for subsequent analysis. The selection of appropriate primary features is essential, as it underpins the robustness and effectiveness of the descriptors discovered through SGD.[14] The importance of each feature was determined by its support score (ss), calculated as [1-Q (with all features except the removed one)/Q (with all features)]. Three categories of primary features associated with the metal atom, bulk, and surface were considered based on previous studies (Table S7).[15] Additional information and specific values for all primary features can be found in the Supplementary Table 1 and 2.

Table S1. List of DFT-D3 predicted ΔE_{agg}, ΔE_{seg} and gas-induced segregation energies of 27 SAAs with 3d-5d dopants on Au (111) surface. (unit: eV)

SAAs system	ΔE_{agg}	ΔE_{seg}	ΔE_{seg}^{O2}	ΔE_{seg}^{CH4}
Sc	0.78	-0.68	1.47	-0.39
Ti	0.34	-0.98	2.05	-0.73
V	0.37	-0.79	1.71	-0.47
Cr	0.30	-0.39	0.98	-0.26
Mn	2.90	-0.20	-0.42	-0.08
Fe	1.93	-0.27	0.81	-1.42
Co	-0.60	-0.70	0.54	-0.53
Ni	0.04	-0.52	0.26	-0.41
Cu	0.11	-0.51	-0.16	-0.41
Zn	0.03	-0.46	0.04	-0.38
Y	1.23	-0.17	1.65	0.15
Zr	0.65	-0.91	2.03	-0.59
Nb	-0.08	-0.84	1.27	-0.55
Mo	-0.86	-0.63	1.83	-0.36
Tc	-0.77	-0.56	1.36	-0.38
Ru	-0.18	-0.53	0.88	-0.26
Rh	0.22	-0.37	0.42	-0.23
Pd	0.07	-0.19	0.04	-0.11
Ag	0.03	-0.05	-0.01	-0.02
Cd	0.11	-0.05	0.04	-0.05
Hf	0.57	-0.97	1.97	-0.71
Ta	0.06	-1.04	1.09	-0.84
W	-1.15	-1.01	1.12	-0.78
Re	-1.37	-0.80	1.37	-0.60
Os	-0.75	-0.68	0.91	-0.43
Ir	0.09	-0.41	0.52	-0.29
Pt	0.02	-0.23	0.06	-0.17

Table S2. List of DFT-D3 predicted ΔE_{agg}, $\Delta E_{seg}$and gas-induced segregation energies of 27 SAAs with 3d-5d dopants on Au (100) surface. (unit: eV)

SAAs system	ΔE_{agg}	ΔE_{seg}	ΔE_{seg}^{O2}	ΔE_{seg}^{CH4}
Sc	0.74	-0.58	1.92	-0.25
Ti	0.17	-1.16	2.23	-0.81
V	0.22	-0.89	1.86	-0.57
Cr	0.17	1.04	2.46	1.17
Mn	0.30	1.47	1.22	1.62
Fe	0.18	-0.43	0.60	-0.30
Co	-0.26	-0.34	1.14	-0.18
Ni	0.13	-0.61	0.18	-0.59
Cu	0.08	-0.54	-0.10	-0.48
Zn	0.05	-0.25	0.38	-0.17
Y	1.21	0.07	2.09	0.42
Zr	0.39	-1.20	2.27	-0.78
Nb	-0.93	-1.36	2.11	-1.00
Mo	-1.75	-0.90	0.85	-0.79
Tc	-1.42	-0.62	0.95	-0.83
Ru	-0.53	-0.86	0.42	-0.77
Rh	0.16	-0.70	0.02	-0.62
Pd	0.15	-0.32	-0.31	-0.27
Ag	0.03	0.01	-0.11	0.01
Cd	0.20	0.20	0.53	0.25
Hf	0.58	-1.23	2.32	-0.88
Ta	-0.29	-1.42	*	-1.29
W	-2.26	-1.56	1.67	-1.25
Re	-2.40	-1.22	0.58	-1.17
Os	-1.71	-1.25	0.44	-1.01
Ir	-0.09	-0.82	0.07	-0.75
Pt	0.12	-0.42	-0.26	-0.38

* indicates that the adsorbed species are unstable on these active sites

Table S3. List of E_{ads} for SAAs under the adsorption of *OOH and H_2O_2 on Au (111) surface. (unit: eV)

SAAs system	ΔE_{ads}^{*OOH}	ΔE_{ads}^{H2O2}
Sc	*	*
Ti	*	*
V	*	*
Cr	*	*
Fe	*	*
Ni	-1.40	*
Cu	-1.27	*
Zn	-1.47	*
Y	-2.79	*
Zr	-3.38	*
Nb	*	*
Ru	-1.58	*
Rh	-1.26	*
Pd	-1.01	-0.57
Ag	-1.01	-0.53
Cd	-1.07	-0.59
Hf	-3.41	*
Ta	*	*
Ir	-1.30	*
Pt	-0.95	*

* indicates that the adsorbed species are unstable on these active sites

Table S4. List of E_{ads} for SAAs under the adsorption of *OOH and H_2O_2 on Au (100) surface. (unite: eV)

SAAs system	ΔE_{ads}^{*OOH}	ΔE_{ads}^{H2O2}
Sc	*	*
Ti	*	*
V	*	*
Cr	*	*
Mn	*	*
Fe	*	*
Ni	-1.84	*
Cu	-1.46	-0.78
Zn	-1.84	-0.82
Y	*	*
Zr	*	*
Rh	-1.31	*
Pd	-1.08	-0.53
Ag	-1.10	-0.55
Cd	-1.34	-0.64
Hf	*	*
Ir	-1.39	*

* indicates that the adsorbed species are unstable on these active sites

Table S5. List of E_{ads} for SAAs under the adsorption of CH_3^* on Au (111) surface. (unite: eV)

SAAs system	ΔE^{*CH3}_{ads}
Sc	-1.63
Ti	-2.15
V	-1.93
Cr	-0.46
Mn	-1.81
Fe	-1.86
Co	-2.09
Ni	-1.86
Cu	-1.53
Zn	-1.65
Y	-1.41
Zr	-2.15
Nb	-2.35
Mo	-2.23
Tc	-2.31
Ru	-2.19
Rh	-2.07
Pd	-1.72
Ag	-1.21
Cd	-1.34
Hf	-2.22
Ta	-2.51
W	-2.53
Re	-2.57
Os	-2.50
Ir	-2.39
Pt	-2.13

Table S6. List of Eads for SAAs under the adsorption of CH_3^* on Au (100) surface. (unite: eV)

SAAs system	ΔE_{ads}^{*CH3}
Sc	-1.97
Ti	-2.42
V	-2.11
Cr	-1.84
Mn	-1.84
Fe	-1.92
Co	-1.91
Ni	-1.80
Cu	-1.43
Zn	-1.71
Y	-1.71
Zr	-2.56
Nb	-2.59
Mo	-2.30
Tc	-2.11
Ru	-2.29
Rh	-2.22
Pd	-1.61
Ag	-1.06
Cd	-1.39
Hf	-2.65
Ta	-2.65
W	-2.79
Re	-2.66
Os	-2.75
Ir	-2.54
Pt	-2.07

Table S7. Considered Features of host and guest.

Abbreviation	Name
IP	Ionization potential of guest (eV)
IPH	Ionization potential of host (eV)
EA	Electron affinity of guest (eV)
EAH	Electron affinity of host (eV)
H	Energy of the highest-occupied Kohn-Sham level for guest (eV)
L	Energy of the lowest-unoccupied Kohn-Sham level for guest (eV)
HH	Energy of the highest-occupied Kohn-Sham level for host (eV)
LH	Energy of the lowest-unoccupied Kohn-Sham level for host (eV)
DC	d-band center of guest (eV)
DCH	d-band center of host (eV)
DTH	d-band center of the top surface layer for host (eV)
DSH	d-band center of the subsurface layer for host (eV)
FH	Slab Fermi level of host (eV)
EC	Cohesive energy of guest (eV)
ECH	Cohesive energy of host (eV)
EB	Binding energy of host metal dimers of guest (eV)
EBH	Binding energy of host metal dimers of host (eV)
dd	Binding distance of guest metal dimers (Å)
ddH	Binding distance of host metal dimers (Å)
RH	Atomic radius of host (Å)

R	Atomic radius of guest (Å)

Table S8. List of energy changes of elementary reaction steps for the production of H_2O_2 in-situ with O_2 on all picked systems. (unite: eV)

SAA/Au(111)	$O_2 + H^* \rightarrow OOH^*$	$OOH^* + H^* \rightarrow H_2O_2$
Pd	-1.25	-1.24
Ag	-0.69	-1.62
Cd	-1.13	-1.22
SAA/Au(100)	$O_2 + H^* \rightarrow OOH^*$	$OOH^* + H^* \rightarrow H_2O_2$
Ag	-0.85	0.84
Cd	-0.60	0.69
Cu	-0.54	0.77
Zn	-0.40	0.70

Table S9. List of energy changes of elementary reaction steps for the conversion of CH_4 to CH_3OH on all picked systems. (unite: eV)

SAA/Au(111)	$CH_4 + OH^* \rightarrow CH_3^* + H_2O$	$CH_3^* + OH^* \rightarrow CH_3OH^*$
Mn	1.31	-1.12
Rh	-0.91	-0.96
Pd	-0.62	-1.16
Ag	-0.03	-1.67
Cd	-0.02	-1.56
Pt	-1.08	-0.77
SAA/Au(100)	$CH_4 + OH^* \rightarrow CH_3^* + H_2O$	$CH_3^* + OH^* \rightarrow CH_3OH^*$
Sc	0.35	-1.25
Cr	-0.12	1.37
Mn	-0.06	-0.16
Zn	0.16	-0.25
Pd	0.29	-0.38
Ag	0.74	-1.01
Cd	0.32	-0.86

Table S10. Elementary-step barriers of the co-doped Pd-Rh/Au (111) tandem models. (unite: eV)

Model-Site	Elementary step	Barriers
Pd	$O_2 + H^* \rightarrow OOH^*$	0.03
Pd	$OOH^* + H^* \rightarrow H_2O_2$	/
Rh	$CH_4 + OH^* \rightarrow CH_3^* + H_2O$	0.43
Rh	$CH_3^* + OH^* \rightarrow CH_3OH^*$	0.76

Table S11. The adsorption energies (E_{ads}) of CH_3OH and the reaction energies (ΔE_{overox}) of the first elementary step in the deep oxidation pathway ($CH_3OH \rightarrow CH_2OH + H^*$) on the relevant surfaces. (unite: eV)

System	$E_{ads}(CH_3OH)$	ΔE_{overox} ($CH_3OH \rightarrow CH_2OH^* + H^*$)
Rh/Au (111)	-0.60	-0.31
Pd-Rh/Au (111)	-0.62	0.05

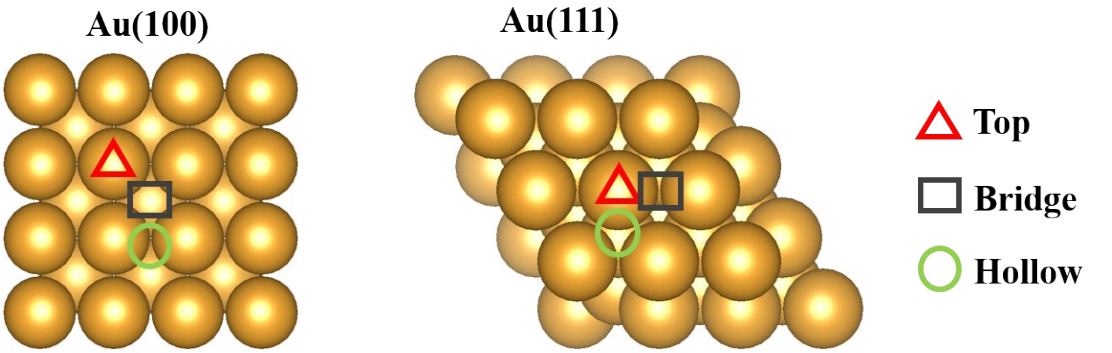

Fig. S1. The different adsorption sites of O_2 and CH_4 on the Au(100) and Au(111) surfaces, respectively.

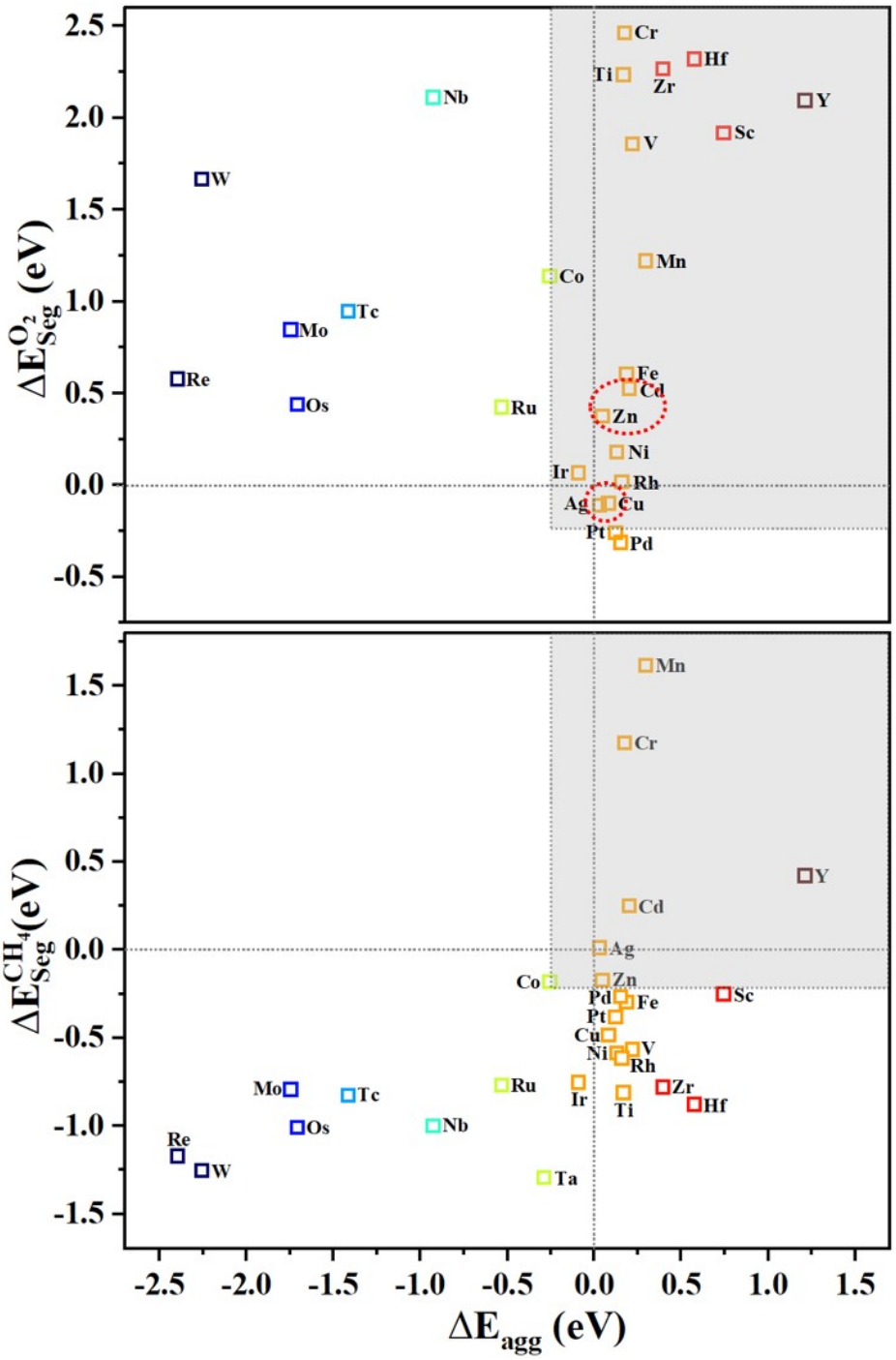

Fig. S2. The plot shows the relationship between segregation and aggregation energies for 27 SAAs based on 3d-5d transition metals dispersed on Au (100) surface. The gray region highlights the regime where an SAA is expected to form, assuming both energies remain positive after including a 0.25 eV entropic correction.

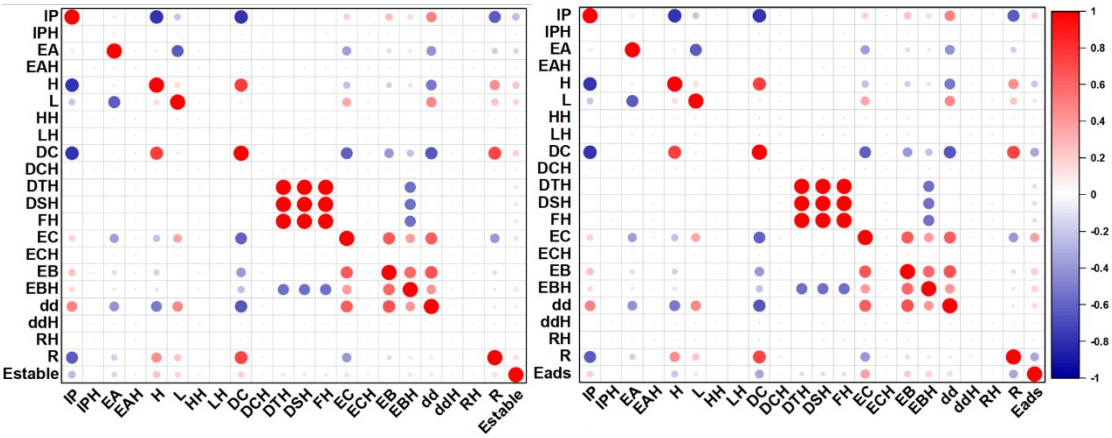

Fig. S3. Correlation heat map of features and properties.

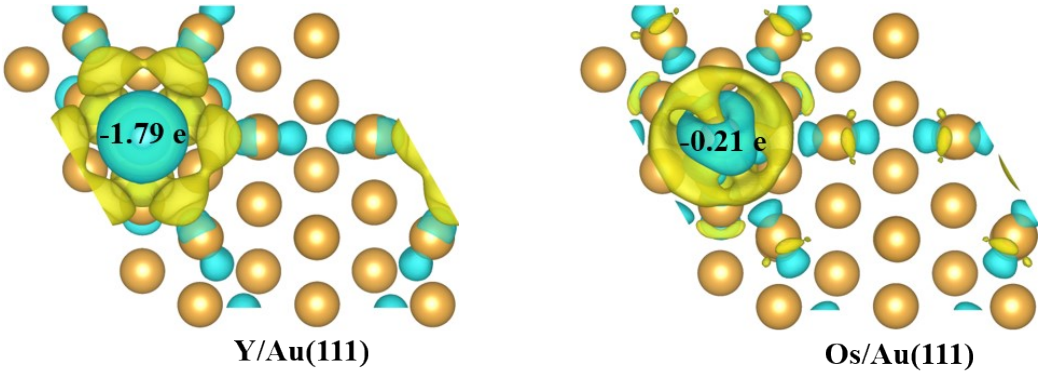

Fig. S4. Top views of differential charge density and Bader charge of the Y and Os SAAs supported on Au (111). The yellow and blue regions indicate electron accumulation and depletion, respectively (isosurface level: 0.0025 e/Å^3).

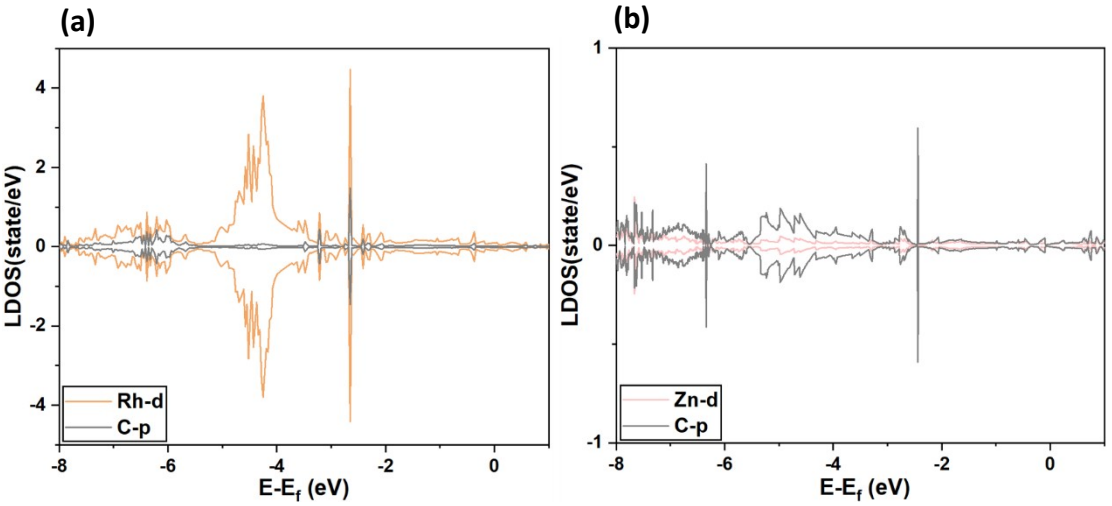

Fig. S5. (a) Local density of states of Rh and C in Rh SAA. (b) Local density of states of Zn and C in Zn SAA.

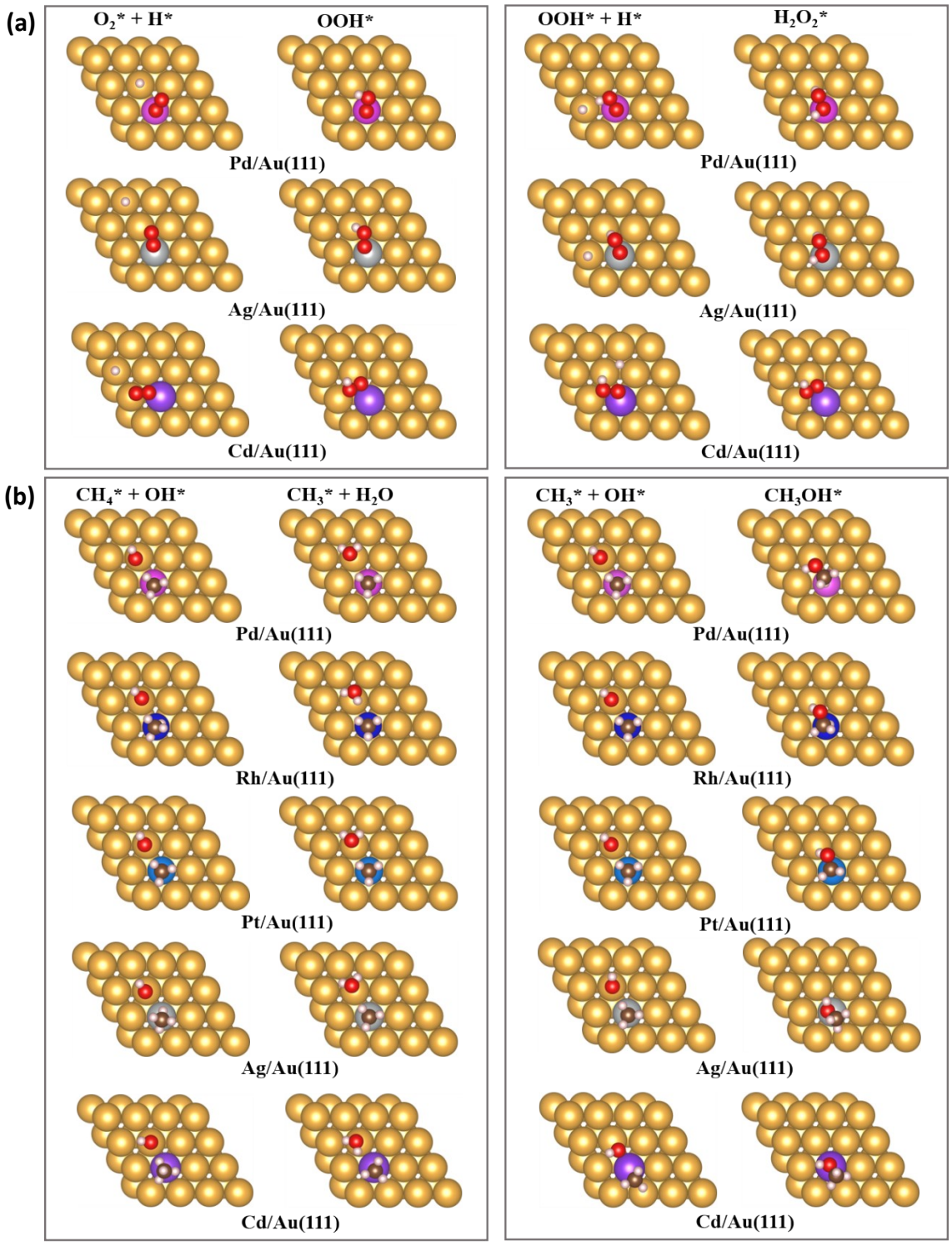

Fig. S6. The optimized structures of the initial and final states over Au (111) loaded SAAs during the tandem reaction of (a) the production of H_2O_2 and (b) the conversion of CH_4 to CH_3OH.

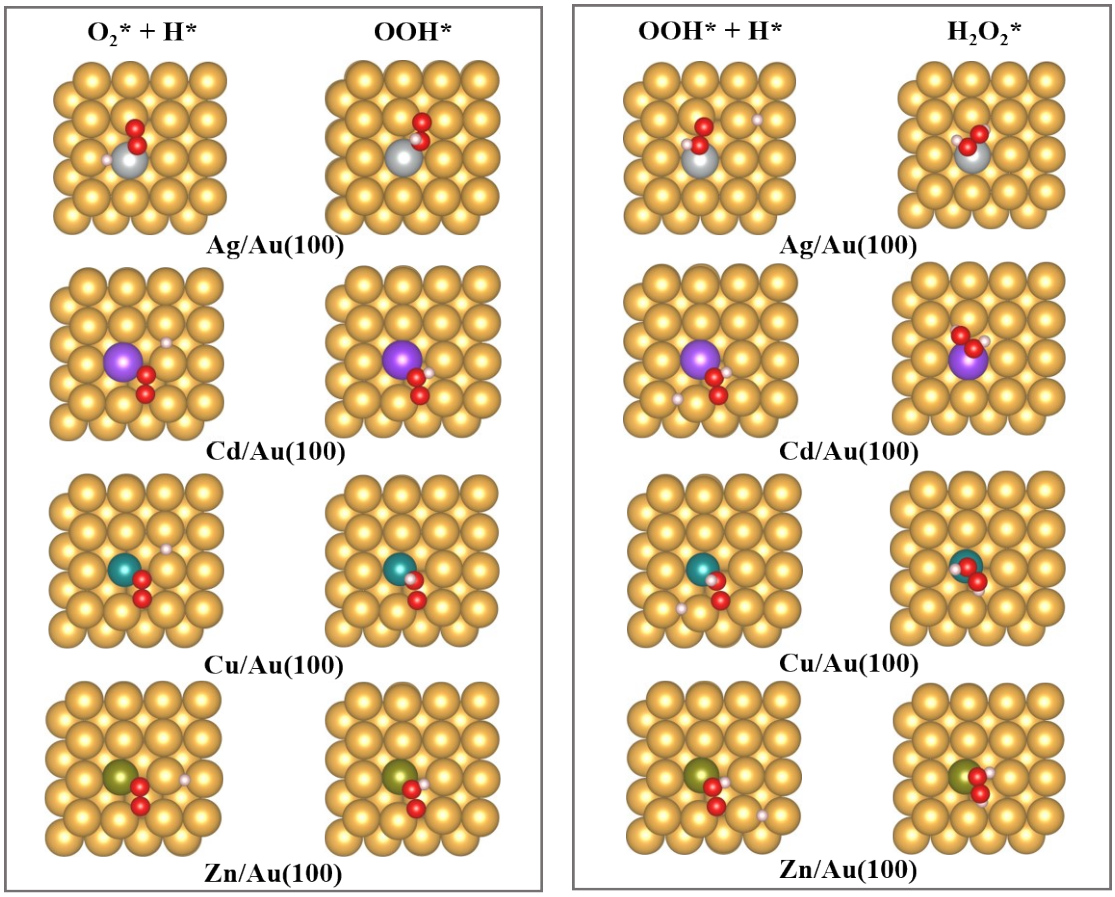

Fig. S7. The optimized structures of the initial and final states over Au (100) loaded SAAs for the production of H_2O_2.

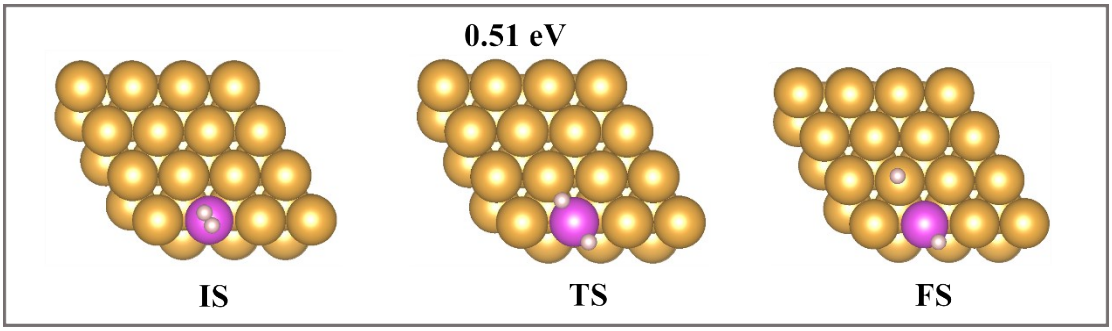

Fig. S8. The optimized initial, transition, and final states (IS, TS, and FS) of H_2 dissociation on Pd/Au (111).

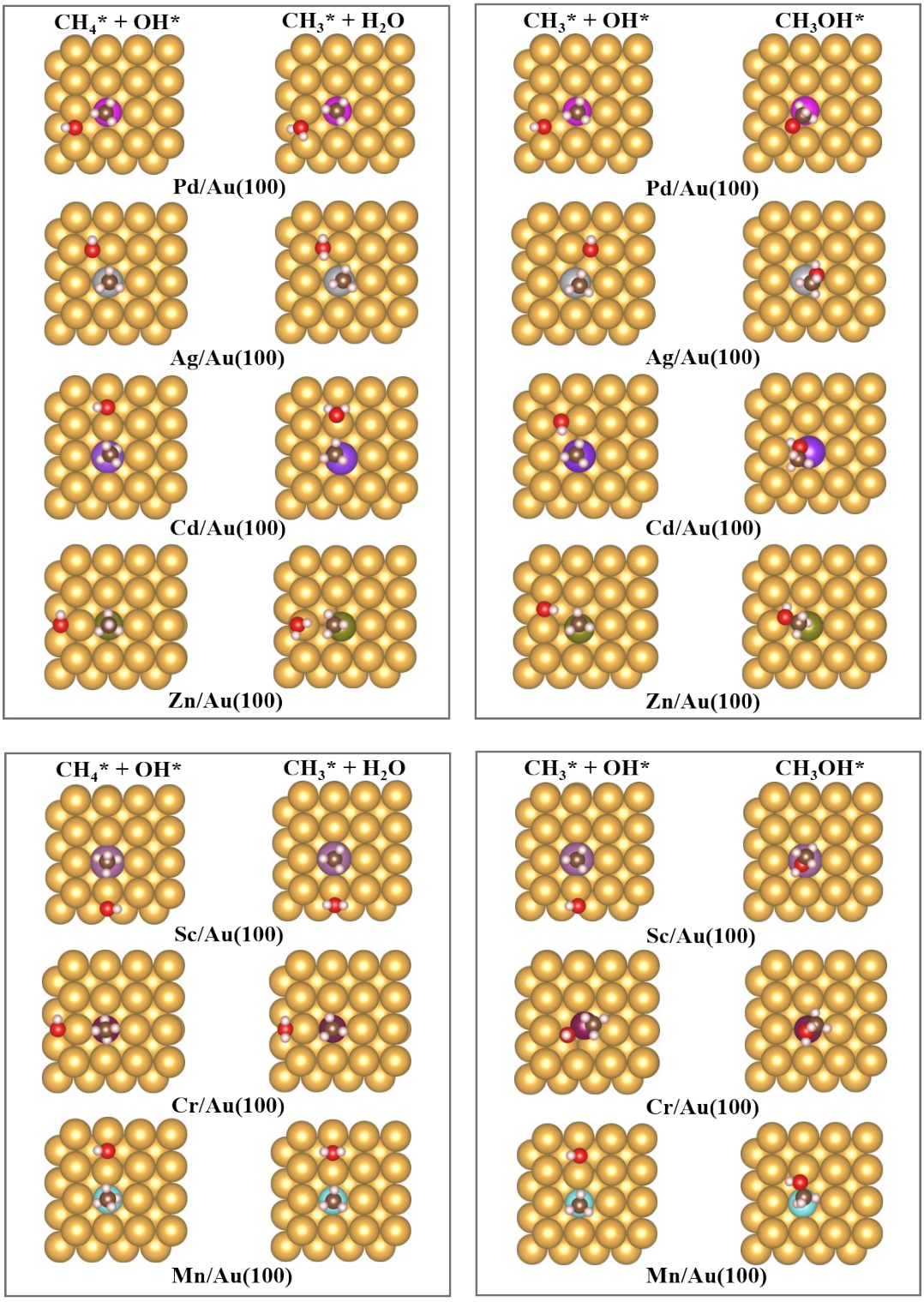

Fig. S9. The optimized structures of the initial and final states over Au (100) loaded SAAs for the conversion of CH_4 to CH_3OH.

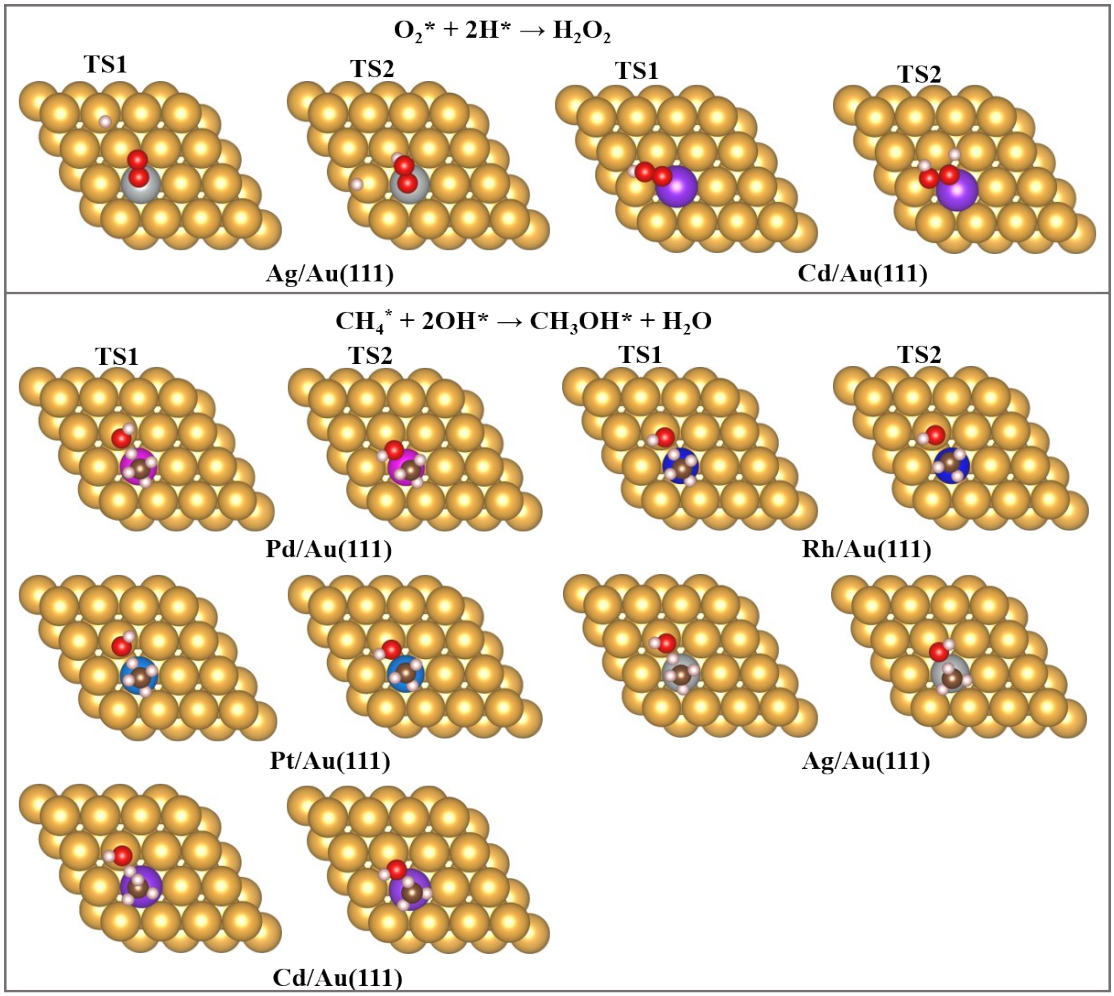

Fig. S10. The structures of the transition states over Au (111) loaded SAAs during the tandem reaction of (a) the production of H_2O_2 and (b) the conversion of CH_4 to CH_3OH.

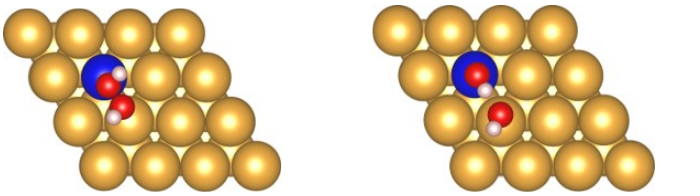

Fig. S11. Starting from a molecularly adsorbed H_2O_2 configuration, structural optimization yields a dissociated OH-derived state on Rh/Au (111).

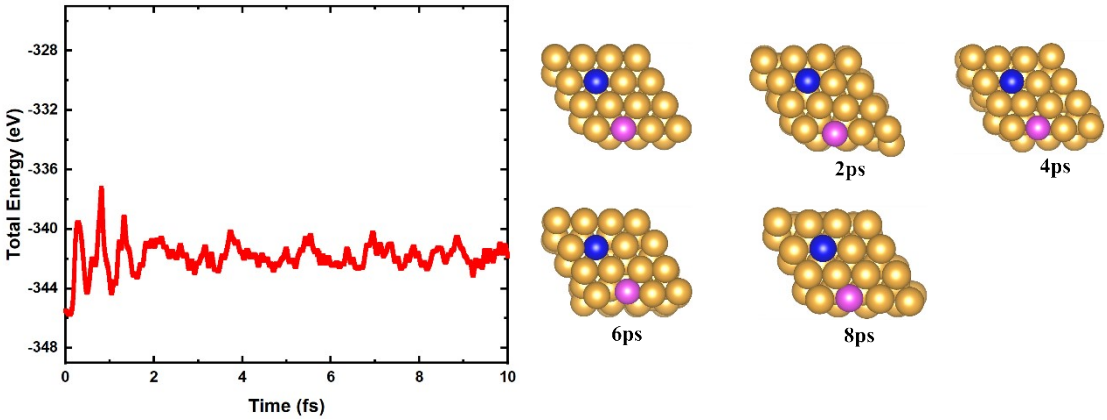

Fig. S12. Energy evolution with simulation time and representative AIMD snapshots of the Pd-Rh/Au (111) tandem motif under vacuum.

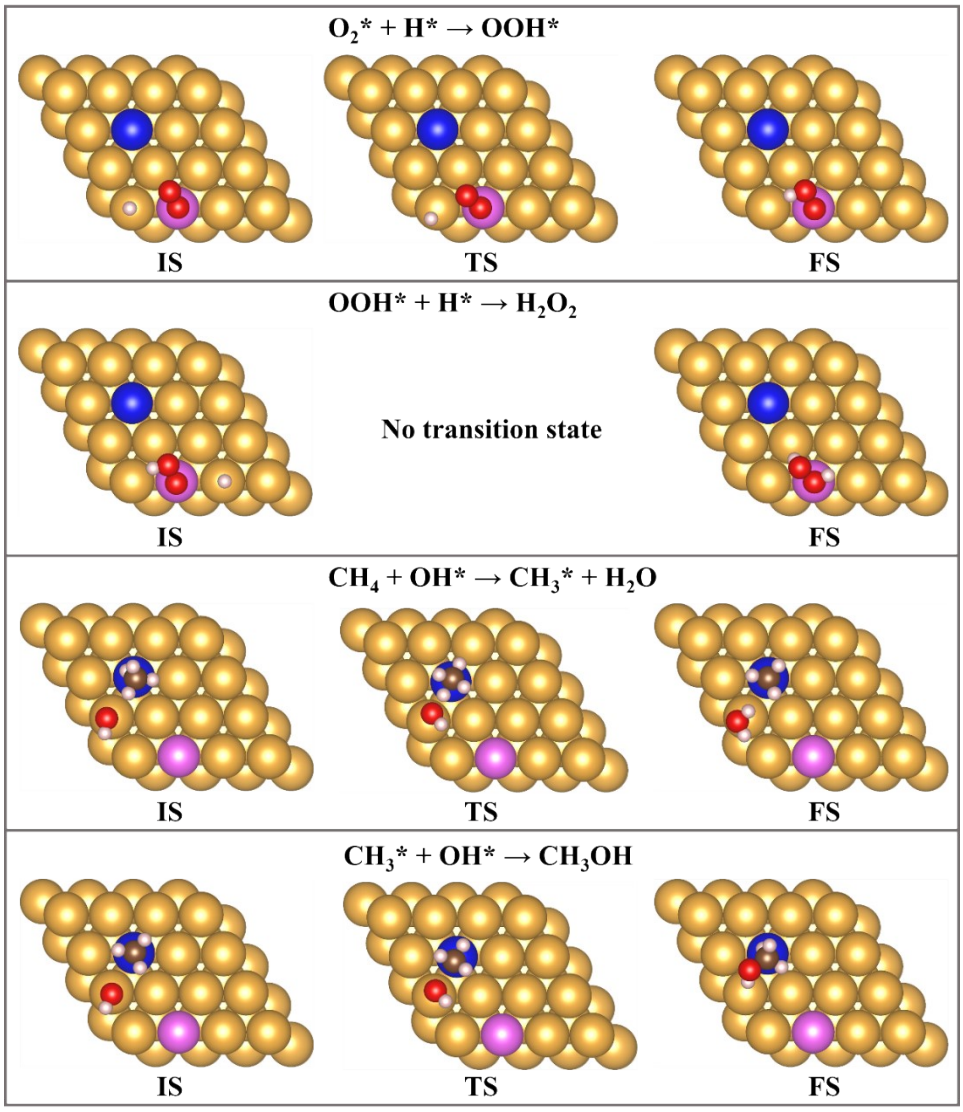

Fig. S13. Optimized initial (IS), transition, and final states (FS) for the production of H_2O_2 on Pd site and the conversion of CH_4 to CH_3OH on Pd site of Pd-Rh/Au (111) tandem motif.

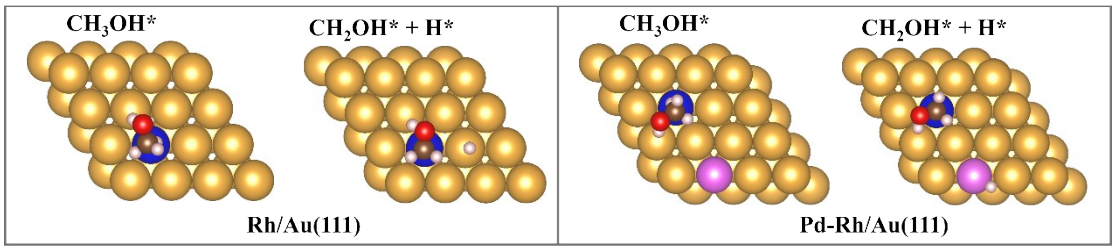

Fig. S14. Optimized structures of the first elementary step in the deep oxidation pathway ($CH_3OH \rightarrow CH_2OH^* + H^*$).

Reference

1. G. Kresse, J. Furthmüller, *Comput. Mater. Sci.,* 1996, **6,** 15-50.
2. G. Kresse, J. Furthmüller, *Phys. Rev. B,* 1996, **54,** 11169-11186.
3. J. P. Perdew, *Phys. Rev. Lett.,* 2008, **100,** 136406.
4. S. Grimme, J. Antony, S. Ehrlich and S. Krieg, *J. Chem. Phys.,* 2010, **132,** 154104.
5. P. E. Blöchl, *Phys. Rev. B,* 1994, **50,** 17953-17979.
6. G. Kresse, D. Joubert, *Phys. Rev. B,* 1999, **59,** 1758-1775.
7. H. J. Monkhorst, J. D. Pack, *Phys. Rev. B,* 1976, **13,** 5188.
8. R. T. Hannagan, G. Giannakakis and E. C. H. Sykes, *Chem. Rev.* 2020, **120,** 12044.
9. M. T. Darby, E. C. H. Sykes and M. Stamatakis, *Top. Catal.,* 2018, **61,** 428.
10. Q. Fu, Y. Luo, *J. Phys. Chem. C,* 2013, **117,** 14618-14624.
11. Y. Lei, Y. Wang, Y. Liu, *Angew. Chem. Int. Ed.,* 2020, **59,** 20794- 20812.
12. G. Henkelman, B. P. Uberuaga,H. J. Jónsson, *Chem. Phys.,* 2000, **113,** 9901-9904.
13. A. Mazheika,Y. G. Wang and M. Scheffler, *Nat. Commun.,* 2022, **13,** 419.
14. B. R. Goldsmith, M. Boley and M. Scheffler, *N. J. Phys.,* 2017, **19,** 013031.
15. Z. K. Han, D. Sarker and R. Ouyang, *Nat. Commun.,* 2021, **12,** 1833.